

## Article

# G-C<sub>3</sub>N<sub>4</sub> Dots Decorated with Hetaerolite: Visible-Light Photocatalyst for Degradation of Organic Contaminants

Zahra Lahootifar<sup>1</sup>, Aziz Habibi-Yangjeh<sup>1,\*</sup>, Shima Rahim Pouran<sup>2</sup> and Alireza Khataee<sup>3,4</sup><sup>1</sup> Department of Chemistry, Faculty of Science, University of Mohaghegh Ardabili, Ardabil 56199-11367, Iran<sup>2</sup> Social Determinants of Health Research Center, Department of Environmental and Occupational Health, Ardabil University of Medical Sciences, Ardabil 85991-56189, Iran<sup>3</sup> Research Laboratory of Advanced Water and Wastewater Treatment Processes, Department of Applied Chemistry, Faculty of Chemistry, University of Tabriz, Tabriz 16471-51666, Iran<sup>4</sup> Department of Environmental Engineering, Faculty of Engineering, Gebze Technical University, Gebze 41400, Turkey

\* Correspondence: ahabibi@uma.ac.ir

**Abstract:** In this paper, a facile hydrothermal approach was used to integrate graphitic carbon nitride dots (CNDs) with hetaerolite (ZnMn<sub>2</sub>O<sub>4</sub>) at different weight percentages. The morphology, microstructure, texture, electronic, phase composition, and electrochemical properties were identified by field emission scanning electron microscopy (FESEM), X-ray photoelectron spectroscopy (XPS), transmission electron microscopy (TEM), high-resolution TEM (HRTEM), energy dispersive X-ray spectroscopy (EDX), X-ray diffraction (XRD), Fourier transform-infrared (FT-IR), ultraviolet-visible diffuse reflectance (UV-vis DR), photoluminescence (PL), electrochemical impedance spectroscopy (EIS), Brunauer–Emmett–Teller (BET), Barrett–Joyner–Halenda (BJH), and photocurrent density. The results of XRD, FT-IR, EDX, and XPS analyses confirmed the synthesis of CNDs/ZnMn<sub>2</sub>O<sub>4</sub> (20%) nanocomposite. As per PL, EIS, and photocurrent outcomes, the binary CNDs/ZnMn<sub>2</sub>O<sub>4</sub> nanocomposite revealed superior features for interfacial transferring of charge carriers. The developed p–n heterojunction at the interface of CNDs and ZnMn<sub>2</sub>O<sub>4</sub> nanoparticles partaken a significant role in the impressive charge segregation and migration. The binary nanocomposites were employed for the photodegradation of several dye pollutants, including rhodamine B (RhB), fuchsin, malachite green (MG), and methylene blue (MB) at visible wavelengths. Amongst the fabricated photocatalysts, the CNDs/ZnMn<sub>2</sub>O<sub>4</sub> (20%) nanocomposite gave rise to about 98% RhB degradation efficiency within 45 min with the rate constant of  $747 \times 10^{-4} \text{ min}^{-1}$ , which was 66.5-, 3.44-, and 2.72-fold superior to the activities of CN, CNDs, and ZnMn<sub>2</sub>O<sub>4</sub> photocatalysts, respectively. The impressive photodegradation performance of this nanocomposite was not only associated with the capacity for impressive visible-light absorption and boosted separation and transport of charge carriers, but also with its large surface area.

**Keywords:** graphitic carbon nitride dots; ZnMn<sub>2</sub>O<sub>4</sub>; p-n heterojunction photocatalyst; organic pollutants

**Citation:** Lahootifar, Z.; Habibi-Yangjeh, A.; Rahim Pouran, S.; Khataee, A. G-C<sub>3</sub>N<sub>4</sub> Dots Decorated with Hetaerolite: Visible-Light Photocatalyst for Degradation of Organic Contaminants. *Catalysts* **2023**, *13*, 346. <https://doi.org/10.3390/catal13020346>

Academic Editor: Meng Li

Received: 5 January 2023

Revised: 27 January 2023

Accepted: 27 January 2023

Published: 3 February 2023



**Copyright:** © 2023 by the authors. Licensee MDPI, Basel, Switzerland. This article is an open access article distributed under the terms and conditions of the Creative Commons Attribution (CC BY) license (<https://creativecommons.org/licenses/by/4.0/>).

## 1. Introduction

Over the past few decades, the shortage of energy and water pollution issues raised by organic compounds have become global concerns of the scientific community [1]. Among the primary water pollutants are organic dyes, which have been a considerable part of water pollution due to their high consumption rate in various industries and resistance to biodegradation. To tackle the detrimental effects of these organic molecules on human health and the environment [2], especially on marine life, numerous advanced materials [3] and strategies have been developed and implemented over time. In particular, the focus has been paid to bio-compatible materials and practical strategies, in addition to being effective and efficient from energy and cost perspectives [2,3]. Advanced oxidation processes (AOPs) are on top of the wastewater treatment techniques that can fulfill the effective degradation

of various organic pollutants [4]. The visible-light-driven heterogeneous photocatalysis is of particular interest among AOPs, since it uses solar energy to drive oxidation reactions for the degradation of organic molecules and eco-clean energy generation [5]. In this regard, the utilized photocatalyst undertakes the central role because its optical, structural, and surface properties chiefly determine the efficiency of a photocatalytic system [6].

On account of the appropriate energy band edges and band gap, tunable electronic structure, high stability, and biocompatibility, graphitic carbon nitride (CN) quickly became the subject of research for various photocatalytic reactions, including CO<sub>2</sub> reduction, synthesis of organic compounds, hydrogen production, removal of pollutants, and nitrogen fixation [7–9]. Nonetheless, the solar-light utilization ability of pristine CN is poor and generates an inefficient amount of charge carriers. Moreover, the rapid recombination of electron/hole pairs, insufficient surface-active centers, and low conductivity confine its practical applications [10]. Hence, numerous attempts have been made to improve the activity of CN through some structural/morphological modifications or heterojunction/s development by integration with other semiconductor/s [11]. Recently, dots and quantum dots of CN have received much interest due to their high disperse ability, quantum confinement effect, and improved heterojunction construction, in addition to the intrinsic properties of the bulk CN [12,13]. For example, Ma et al. realized that anchoring CN quantum dots on 2D g-C<sub>3</sub>N<sub>4</sub> improved photocatalytic activity [13]. Moreover, the latest research activities on the improvement of carbon nitride photocatalytic activity have been reviewed [14,15].

Spinel zinc manganese oxide (ZnMn<sub>2</sub>O<sub>4</sub>, E<sub>g</sub> = 1.70 eV) is a p-type semiconductor active in the visible region. Among spinels, ZnMn<sub>2</sub>O<sub>4</sub> has attracted much attention due to its outstanding technological importance as catalyst, solid electrolyte, etc., [16]. Reduction in CO<sub>2</sub> and destruction of pollutants are photocatalytic applications of this spinel [16].

Among water pollutants, rhodamine B (RhB), with carcinogenic and neurotoxic properties, has a high potential to cause diseases in humans [17]. Fushin can affect the central nervous system and cause drowsiness and dizziness in humans [18]. Malachite Green (MG) is a carcinogenic and mutagenic agent in living organisms [19]. Moreover, methylene blue (MB) has a severe impact on human health and the environment, because it is carcinogenic and non-biodegradable in nature. Among the dangers of MB, its effect on the respiratory system, blindness, digestive and mental disorders, shock, gastritis, jaundice, tissue necrosis, and an increase in heart rate has been highlighted [20].

The appealing properties of CN dots (CNDs) and complementary characteristics of ZnMn<sub>2</sub>O<sub>4</sub> brought the idea of designing a binary heterostructure based on these semiconductors. For this purpose, a hydrothermal method was used to deposit various weight percentages of ZnMn<sub>2</sub>O<sub>4</sub> nanoparticles over CNDs. The photocatalytic activities were also determined for the degradation of several organic dye contaminants, including RhB, fuchsin, MG, and MB molecules. Finally, the nanocomposite with the best optical and photocatalytic activity was introduced, and the corresponding degradation mechanism was suggested.

## 2. Results and Discussions

The fabricated CN, CNDs, ZnMn<sub>2</sub>O<sub>4</sub>, and CNDs/ZnMn<sub>2</sub>O<sub>4</sub> (20%) materials were characterized by XRD to expose the corresponding crystalline phases (Figure 1a). In the pattern of CN, two sharp peaks appeared at 2θ values of 13.1° and 27.4° (JCPDS No. 01-087-1526), corresponding to stacking between the surfaces of the CN layers [21]. The pattern of CNDs shows only one peak at 27.4°, indicating that CNDs has the same intrinsic crystal structure as CN. The peak at 13.1° disappeared and the intensity of the peak at 27.4° diminished compared to CN. This decrease is due to the small size of CNDs particles [22]. On the other hand, the peaks appeared at 2θ = 18.62°, 29.47°, 31.42°, 33.22°, 36.47°, 39.27°, 44.77°, 52.22°, 54.42°, 56.87°, 58.98°, 60.92°, and 65.25°, respectively, correspond to the reflections from (101), (112), (200), (103), (211), (004), (220), (105), (312), (303), (321), (224), and (400) planes of ZnMn<sub>2</sub>O<sub>4</sub> (JCPDS file No. 01-077-0470) [23]. The XRD pattern of

CNDs/ZnMn<sub>2</sub>O<sub>4</sub> (20%) nanocomposite included all the diffraction peaks relevant to CNDs and the tetragonal phase of ZnMn<sub>2</sub>O<sub>4</sub>, indicating the accuracy of the synthesis procedure. According to the correct position of the XRD peaks, it is concluded that the synthesis of the nanocomposite has been correctly performed. The surface functional groups of the CNDs/ZnMn<sub>2</sub>O<sub>4</sub> (20%) sample were recorded by FT-IR spectroscopy and elucidated with respect to CN and CNDs spectra (Figure 1b). The CN and CNDs samples gave rise to similar FT-IR spectra. In both of them, the wide-ranging peaks at 2900–3450 cm<sup>-1</sup> assign to the O–H and N–H stretching modes [24]. The peaks that appeared at wavenumbers of 1200–1650 cm<sup>-1</sup> are relevant to the C–N and C=N groups [22,25]. Moreover, the bands related to the atmospheric CO<sub>2</sub> and C–O stretching modes emerged at 2385 cm<sup>-1</sup> and 1060 cm<sup>-1</sup>, respectively [26]. The peak related to the stretching vibration of heptazine units was also identified at 800 cm<sup>-1</sup> [26]. In the case of CNDs/ZnMn<sub>2</sub>O<sub>4</sub> (20%) nanocomposite, not only the peaks attributing to CNDs appeared in the spectrum, but also the peaks assigning to the M–O bonds of the corresponding metal oxides (M = Zn and Mn) showed up at 640 cm<sup>-1</sup> and 545 cm<sup>-1</sup>, respectively [27,28]. Hence, all the functional groups are visible in the figure, which confirmed the synthesis of the binary photocatalyst.

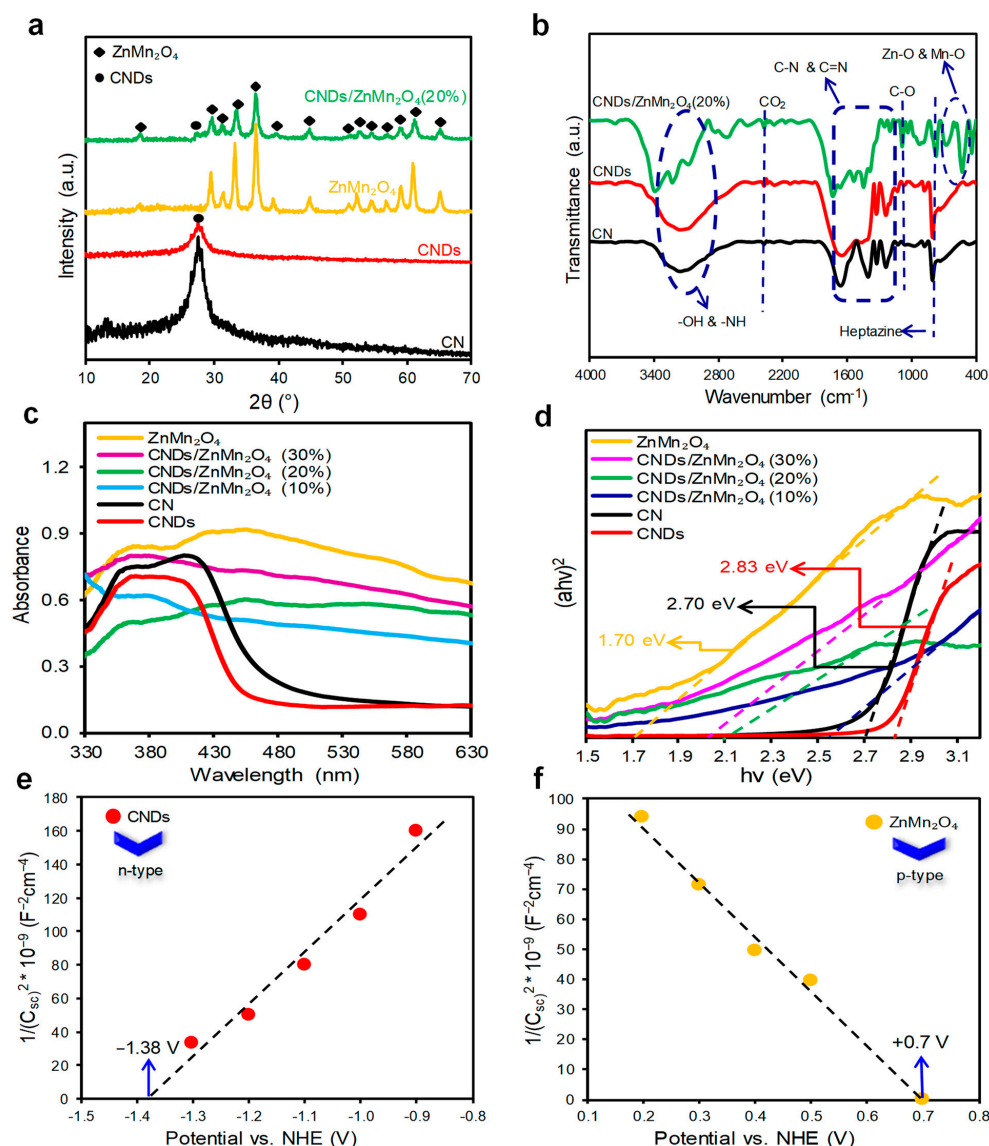


**Figure 1.** (a) XRD, (b) FT-IR, (c) Optical absorbance, (d) Tauc plots, and (e,f) Mott-Schottky plots of the specified samples.

The electronic properties of CN, CNDs,  $\text{ZnMn}_2\text{O}_4$ , and CNDs/ $\text{ZnMn}_2\text{O}_4$  composites were studied through their UV–vis DR spectra (Figure 1c). As per the data, although the CN and CNDs photocatalysts showed absorptions at visible wavelengths, the visible-light absorption capability of CNDs/ $\text{ZnMn}_2\text{O}_4$  nanocomposites is highly promoted following the incorporation of the small band gap  $\text{ZnMn}_2\text{O}_4$  with medium band gap CNDs. The  $E_g$  values were afterward obtained using Tauc's plots [29], which were 2.70, 2.83, 1.70, 2.54, 2.10, and 2.02 eV for CN, CNDs,  $\text{ZnMn}_2\text{O}_4$ , CNDs/ $\text{ZnMn}_2\text{O}_4$  (10%), CNDs/ $\text{ZnMn}_2\text{O}_4$  (20%), and CNDs/ $\text{ZnMn}_2\text{O}_4$  (30%) photocatalysts, respectively (Figure 1d). Moreover, the flat-band potentials and the type of semiconductors were determined via applying the Mott-Schottky (M-S) analysis [30] as illustrated in Figure 1e,f. As noticed, the CNDs and  $\text{ZnMn}_2\text{O}_4$  exhibited n-type and p-type characteristics with a positive and negative slopes, respectively. The calculated  $E_{CB}$  and  $E_{VB}$  values for CNDs were  $-1.48$  eV and  $+1.35$  eV, and for  $\text{ZnMn}_2\text{O}_4$  were  $-0.90$  eV and  $+0.80$  eV, respectively.

The morphological features of the CNDs/ $\text{ZnMn}_2\text{O}_4$  (20%) nanocomposite were studied through FESEM, TEM, and HRTEM images. The FESEM and TEM images of the sample present aggregated particles composed of nearly spherical particles (Figure 2a,b). In the HRTEM image of CNDs/ $\text{ZnMn}_2\text{O}_4$  (20%) nanocomposite presented in Figure 2c, the lattice fringes of CNDs and  $\text{ZnMn}_2\text{O}_4$  were identified with inter-planar distances of 0.340 and 0.490 nm, respectively [22,31]. This figure confirms the combination of CNDs and  $\text{ZnMn}_2\text{O}_4$  components to construct a binary p-n heterojunction photocatalyst. The elements of the binary nanocomposite were detected by EDX analyses (Figure 2d). The C, N, O, Mn, and Zn elements were the only elements identified in the CNDs/ $\text{ZnMn}_2\text{O}_4$  (20%) nanocomposite. The EDX mapping images of the nanocomposite were also collected, which displayed elements with almost homogeneous dispersion in the nanocomposite structure (Figure 2e).

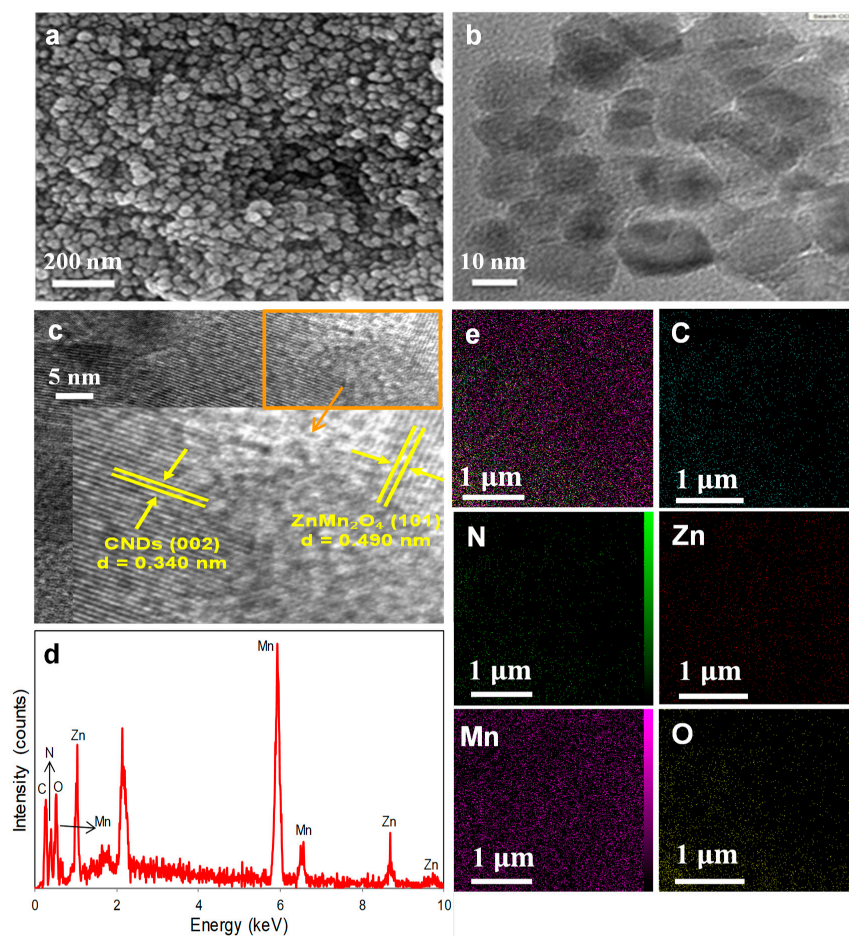


**Figure 2.** (a) SEM, (b) TEM, and (c) HRTEM images. (d) EDX spectrum and (e) EDX mapping of CNDs/ $\text{ZnMn}_2\text{O}_4$  (20%) nanocomposite.

Figure 3 shows the oxidation states of the elements in the CNDs/ZnMn<sub>2</sub>O<sub>4</sub> (20%) nanocomposite as per XPS analysis. The survey spectrum consisted of the peaks related to C 1s, N 1s, Zn 2p, Mn 2p, and O 1s. The narrow scan of carbon was completed in the 283–292 eV region and produced two dominant peaks, which were deconvoluted into three peak components at binding energies (B.E) of 284.7, 285.5, and 288.5 eV, which were, respectively, associated with the sp<sup>2</sup> graphitic carbon (C–C), sp<sup>2</sup> aromatic C attached to –NH<sub>2</sub>, and the carbon corresponded to heptazine/triazazine C–N–C coordination (Figure 3b) [24]. The N 1s spectrum generated in the corresponding narrow scan was deconvoluted into four peak components positioned at 398.5, 399.1, and 400.5 eV (Figure 3c), which correspond to the nitrogen as sp<sup>2</sup>-hybridized (C=N–C), tertiary form (N–(C)<sub>3</sub>) and hydrogen-bonded (C–N–H), respectively [24]. The Zn 2p high-resolution spectrum produced two peaks at B.E. of 1043.6 eV and 1020.5 eV, respectively, matched with Zn 2p<sub>1/2</sub> and Zn 2p<sub>3/2</sub> and indicated the existence of Zn element in +2 oxidation state (Figure 3d) [32]. On the other hand, the Mn 2p narrow scan generated two strong peaks, one associated with Mn 2p<sub>3/2</sub> centered at binding energy of 641.8 eV and the other one ascribed to Mn 2p<sub>1/2</sub> at 653.4 eV (Figure 3e) [32]. The O 1s spectrum deconvolution resulted in three peaks at 530.2, 531.8, and 533 eV, respectively, related to ZnMn<sub>2</sub>O<sub>4</sub> lattice oxygen, surface hydroxyl content, and residual adsorbed H<sub>2</sub>O, respectively (Figure 3f) [31,33].

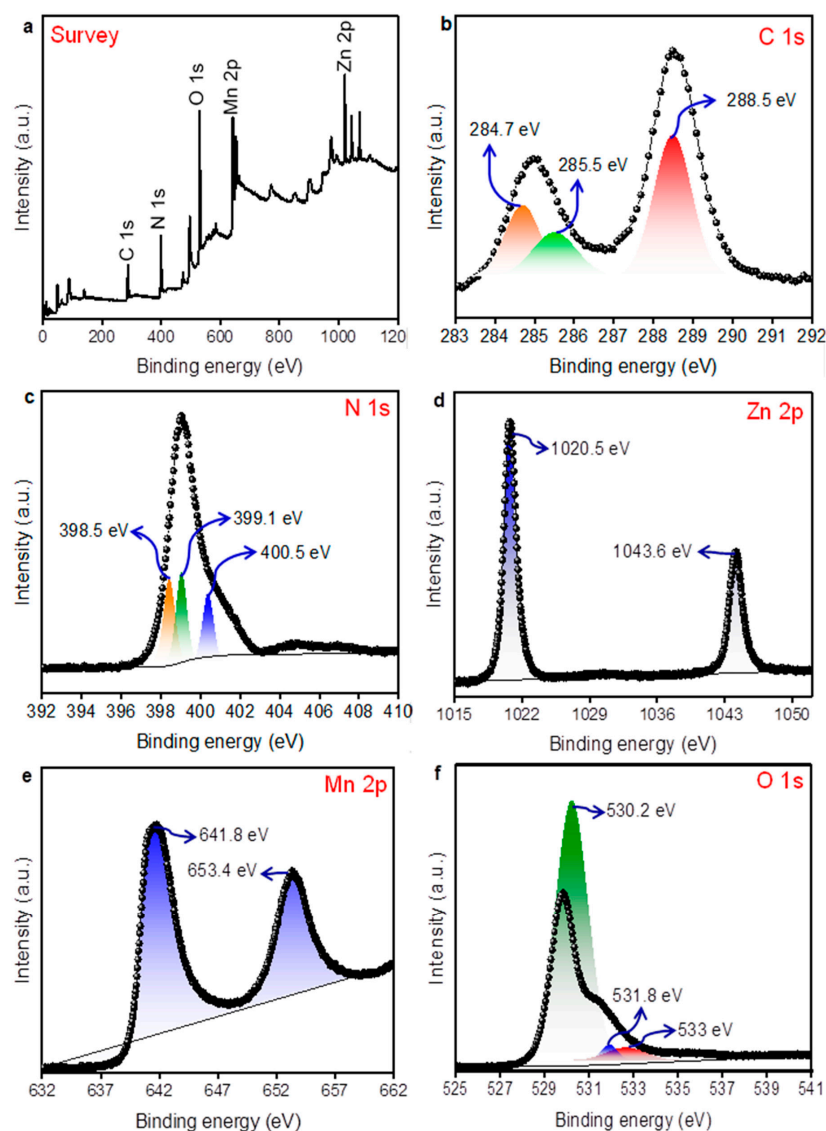


**Figure 3.** XPS spectra of CNDs/ZnMn<sub>2</sub>O<sub>4</sub> (20%) photocatalyst: (a) Survey, (b) C1s, (c) N1s, (d) Zn 2p, (e) Mn 2p, and (f) O1s spectra.

The photocatalytic degradation efficiency of the samples was examined for photo-oxidation of RhB under visible light. Figure 4a depicts the changes in the RhB concentration ( $C_t/C_0$ ) within diverse photocatalytic systems per irradiation period. Prior to the experiments, the adsorption capacity of the samples was investigated through the stirring of the dye solution with the photocatalyst under dark conditions for 60 min. As per results, a negligible amount (8%) of RhB was removed through only light illumination, i.e., the absence of photocatalyst, indicating the inefficacy of visible light in breaking the chemical bonds of RhB molecules. The system including the pristine CN resulted in low RhB removal efficiency of about 20%, which can be strongly associated with the poor harvesting of light in visible region and rapid recombination of charges. However, the CNDs photocatalyst showed much higher activity with removal of 73% at the same time. By contrast, almost complete removal of RhB has been achieved over the CNDs/ZnMn<sub>2</sub>O<sub>4</sub> (20%) nanocomposite within 45 min. The order of photoactivity was as CNDs/ZnMn<sub>2</sub>O<sub>4</sub> (20%) > CNDs/ZnMn<sub>2</sub>O<sub>4</sub> (30%) > CNDs/ZnMn<sub>2</sub>O<sub>4</sub> (10%) > CNDs/ZnMn<sub>2</sub>O<sub>4</sub> (40%) > CNDs/ZnMn<sub>2</sub>O<sub>4</sub> (5%) > ZnMn<sub>2</sub>O<sub>4</sub> > CNDs > CN. The plots of  $\ln(C_0/C)$  vs. time for degradation of RhB over the studied samples revealed that the photocatalytic reactions obeyed the pseudo-first-order kinetic model (see Figure 4b). The rate constants for RhB removal using different photocatalysts were calculated to be  $11.2 \times 10^{-4} \text{ min}^{-1}$  (CN),  $217 \times 10^{-4} \text{ min}^{-1}$  (CNDs),  $275 \times 10^{-4} \text{ min}^{-1}$  (ZnMn<sub>2</sub>O<sub>4</sub>),  $284 \times 10^{-4} \text{ min}^{-1}$  (CNDs/ZnMn<sub>2</sub>O<sub>4</sub> (5%)),  $329 \times 10^{-4} \text{ min}^{-1}$  (CNDs/ZnMn<sub>2</sub>O<sub>4</sub> (40%)),  $333 \times 10^{-4} \text{ min}^{-1}$  (CNDs/ZnMn<sub>2</sub>O<sub>4</sub> (10%)),  $429 \times 10^{-4} \text{ min}^{-1}$  (CNDs/ZnMn<sub>2</sub>O<sub>4</sub> (30%)), and  $747 \times 10^{-4} \text{ min}^{-1}$  (CNDs/ZnMn<sub>2</sub>O<sub>4</sub> (20%)) (Figure 4c). As per results, the nanocomposites showed higher photodegradation rates than pristine CN, wherein the activity of CNDs/ZnMn<sub>2</sub>O<sub>4</sub> (20%) nanocomposite was, respectively, 66.5, 3.44, and 2.72-fold superior to the activities of CN, CNDs, and ZnMn<sub>2</sub>O<sub>4</sub> photocatalysts, respectively. The boosted photocatalytic activities of the binary samples implied that the combination of CNDs with ZnMn<sub>2</sub>O<sub>4</sub> was the right action, which should be taken place with optimum weight percentages.

The reactive species produced in a photocatalytic system are the central elements involved in the photodegradation of organic molecules. To estimate the type of the reactive species, a group of experiments using scavengers, including AOX, BQ, and 2-PrOH was performed to, respectively, probe  $h^+$ ,  $\bullet O_2^-$ , and  $\bullet OH$  species. Figure 4d depicts the RhB photo-oxidation rate constants using the CNDs/ZnMn<sub>2</sub>O<sub>4</sub> (20%) nanocomposite, without or with the scavengers. The rate constant of  $747 \times 10^{-4} \text{ min}^{-1}$ , which was obtained in the absence of the scavengers, was significantly dropped to  $154 \times 10^{-4}$ ,  $53.4 \times 10^{-4}$ , and  $1.03 \times 10^{-4} \text{ min}^{-1}$  upon 2-PrOH, AOX, and BQ supplementation into the system, respectively. As can be inferred from the result, all three probed species contributed to the RhB photodegradation process and their role are as  $\bullet O_2^- > h^+ > \bullet OH$ .

The photocatalytic activities of CN, CNDs, and CNDs/ZnMn<sub>2</sub>O<sub>4</sub> (20%) samples were further examined for degradation of some other dye pollutants, including MG, fuchsin and MB and the outcomes were presented as compared with the RhB results (Figure 4e). As per the results, the highest removal efficiencies of all the studied dyes were achieved over the CNDs/ZnMn<sub>2</sub>O<sub>4</sub> (20%) system. The photoactivity of the binary sample for degradation of RhB, MG, fuchsin, and MB was 66.5, 15.8, 13.2, and 31.2-fold greater than CN, and 3.44, 1.5, 18.1, and 11.5 times premier than CNDs, respectively. Accordingly, the CNDs/ZnMn<sub>2</sub>O<sub>4</sub> (20%) sample showed an outstanding photocatalytic activity for the treatment of various recalcitrant dye wastewater. The binary photocatalyst underwent four consecutive runs under the same operational conditions for RhB removal in order to assess its stability and potential reusability (Figure 4f). As noticed, the CNDs/ZnMn<sub>2</sub>O<sub>4</sub> (20%) nanocomposite demonstrated excellent efficiency for RhB photodegradation under visible light in all the conducted experiments, and the loss of performance was insignificant at the end of the cycle, confirming its significant stability.

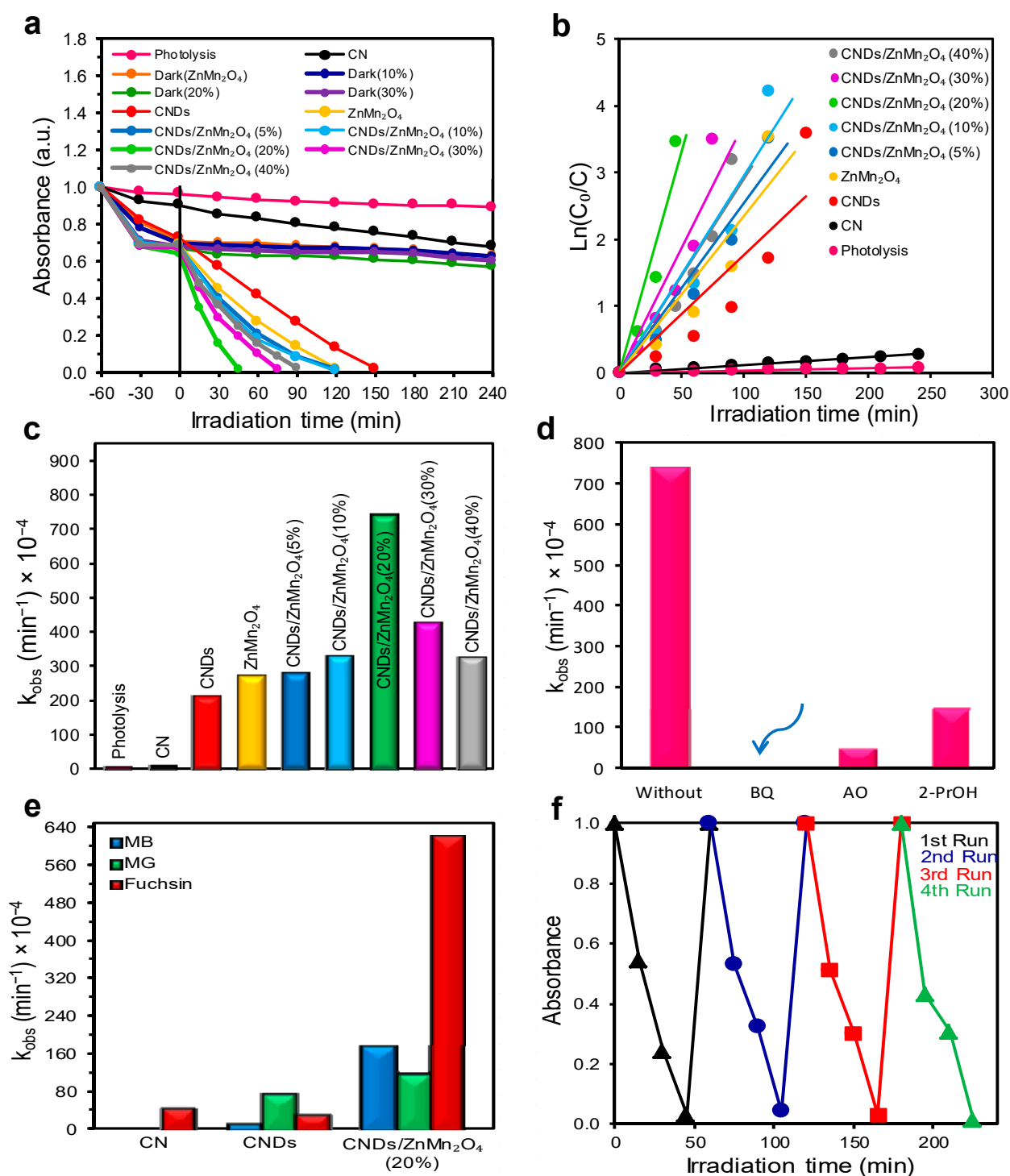


**Figure 4.** (a) RhB photodegradation, (b) First-order-kinetic plots for the degradation rates of RhB, (c) degradation rate constants of RhB, (d) Effect of trapping agents on the degradation of RhB, (e) Degradation constants of MB, MG, and fuchsin, and (f) the results of recycling experiments of CNDs/ZnMn<sub>2</sub>O<sub>4</sub> (20%) system for degradation of RhB.

The ability for adequate segregation and transfer of the photoinduced charge carriers is among the crucial factors connected with immense photocatalytic activities [34]. On this basis, electrochemical impedance spectroscopy, photoluminescence, and photocurrent spectroscopy analyses were conducted to figure out the characteristics of the CNDs/ZnMn<sub>2</sub>O<sub>4</sub> (20%) nanocomposite with respect to the ZnMn<sub>2</sub>O<sub>4</sub>, CNDs, and CN materials. Figure 5a shows the EIS responses of the samples, wherein the least impedance was detected for the

CND<sub>s</sub>/ZnMn<sub>2</sub>O<sub>4</sub> (20%) sample compared to those of ZnMn<sub>2</sub>O<sub>4</sub>, CND<sub>s</sub>, and CN photocatalysts. This indicated the notable reduction in the resistance towards charge transfer in the CND<sub>s</sub>/ZnMn<sub>2</sub>O<sub>4</sub> (20%) nanocomposite. The PL results were also in line with the EIS response of the binary nanocomposite, wherein the weakest PL belonged to the CND<sub>s</sub>/ZnMn<sub>2</sub>O<sub>4</sub> (20%) nanocomposite (Figure 5b). Since the photoluminescence intensity shows the amount of photo energy released from returning the photo-excited material to the ground state, the higher released energy means more recombination of photoinduced charges. As per the results, the CND<sub>s</sub>/ZnMn<sub>2</sub>O<sub>4</sub> (20%) sample had a minimal recombination rate or the best performance for transferring the charge carriers compared to the pristine photocatalysts. The best optical performance of the binary sample was further confirmed via photocurrent analyses, as presented in Figure 5c. The stronger photocurrent intensity of the CND<sub>s</sub>/ZnMn<sub>2</sub>O<sub>4</sub> (20%) photocatalyst in comparison to the CN, CND<sub>s</sub>, and ZnMn<sub>2</sub>O<sub>4</sub> samples indicated its exceptional performance in extending the lifespan of the photoinduced charges. Therefore, the EIS, PL, and photocurrent results confirmed the high potential of the CND<sub>s</sub>/ZnMn<sub>2</sub>O<sub>4</sub> (20%) nanocomposite for photocatalytic applications.

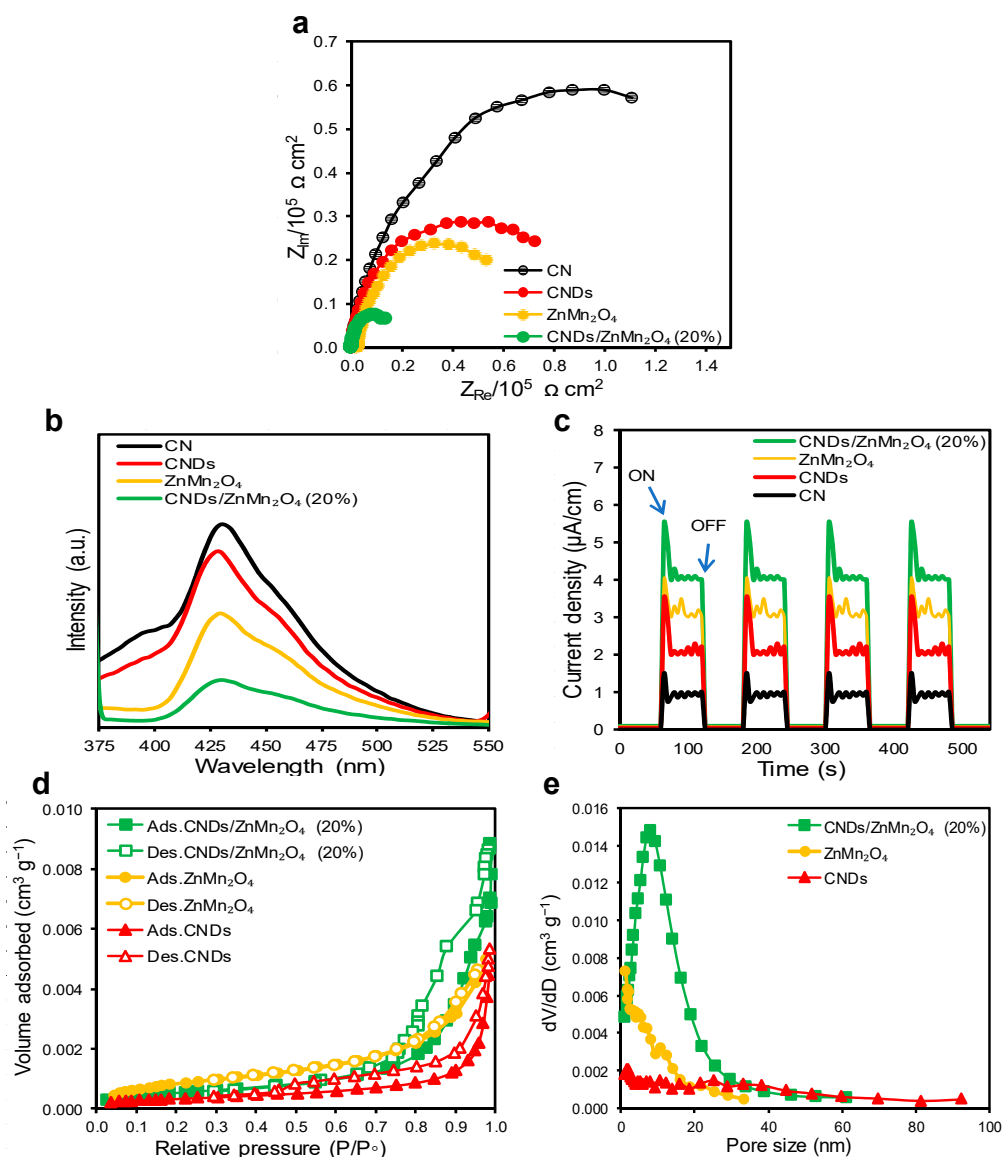


**Figure 5.** (a) EIS, (b) PL, and (c) Photocurrent of CN, CND<sub>s</sub>, ZnMn<sub>2</sub>O<sub>4</sub>, and CND<sub>s</sub>/ZnMn<sub>2</sub>O<sub>4</sub> (20%) photocatalysts. (d) N<sub>2</sub> sorption data and (e) pore-size distributions for CND<sub>s</sub>, ZnMn<sub>2</sub>O<sub>4</sub>, and CNQDs/ZnMn<sub>2</sub>O<sub>4</sub> (20%) photocatalysts.

The surface properties of a photocatalyst are also influential factors as photocatalytic reactions take place on the surface [35]. Moreover, the charge transfer is also affected by surface characteristics. Therefore, the active sites and pore features of the studied photocatalysts were identified via  $N_2$  adsorption–desorption isotherms (Figure 5d,e). From the BET isotherms, the  $N_2$  sorption behavior of CNDs,  $ZnMn_2O_4$ , and CNDs/ $ZnMn_2O_4$  (20%) photocatalysts followed type II with  $H_3$  hysteresis loops. As per the outcomes (Table 1), the integration of CNDs ( $12.03 \text{ m}^2 \text{ g}^{-1}$ ) and  $ZnMn_2O_4$  ( $33.8 \text{ m}^2 \text{ g}^{-1}$ ) contributed to an expanded active surface of the binary sample ( $44.6 \text{ m}^2 \text{ g}^{-1}$ ). The enlarged surface area could play a remarkable role in its promoted photocatalytic activity.

**Table 1.** Textural properties of the CNDs,  $ZnMn_2O_4$ , and CNDs/ $ZnMn_2O_4$  (20%) photocatalysts.

Sample	Surface Area ( $\text{m}^2 \text{ g}^{-1}$ )	Mean Pore Diameter (nm)	Total Pore Volume ( $\text{cm}^3 \text{ g}^{-1}$ )
CNDs	12.03	27.73	0.08
$ZnMn_2O_4$	33.8	9.09	0.08
CNDs/ $ZnMn_2O_4$ (20%)	44.6	27.5	0.31

Based on the outcomes, a mechanism was suggested to illustrate the route through which the pollutant molecules undergo a visible-light photodegradation reaction over the binary CNDs/ $ZnMn_2O_4$  nanocomposites. As a result of the constructed p–n heterojunction between n-type CNDs and p-type  $ZnMn_2O_4$ , the electrons more from the Fermi level of CNDs to that of  $ZnMn_2O_4$  until the Fermi levels reach an equilibrium state, resulting in, respectively, positive and negative charges on CNDs and  $ZnMn_2O_4$  in the junction regions [36,37]. Upon the excitation of CNDs and  $ZnMn_2O_4$  semiconductors by visible light, the electrons on the VBs of both components move to the corresponding CBs, while the holes remain on the VBs (Figure 6). After that, due to the influence of the inner electric field, the electrons on the  $CB_{ZnMn_2O_4}$  rapidly transfer to the  $CB_{CNDs}$ , where they can be trapped by oxygen molecules to produce  $\cdot O_2^-$  and  $\cdot OH$  species. Additionally, the contaminants can get oxidized directly by the holes remaining at the VB of  $ZnMn_2O_4$ . The rapid migration of the photo generated charges can be facilitated via the formed p–n heterojunction, leading to extending the lifetime of the charge carriers and diminishing recombination of them, which is highly beneficial for impressive photocatalytic performance [38,39].

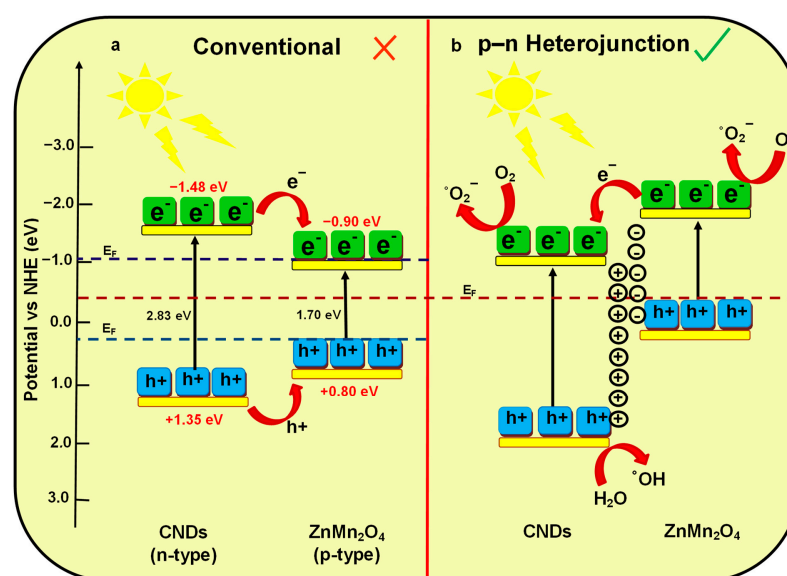


**Figure 6.** Photocatalytic mechanism for improved activity of CNDs/ $ZnMn_2O_4$  nanocomposites: (a) Conventional and (b) p–n Heterojunction.

### 3. Experimental Part

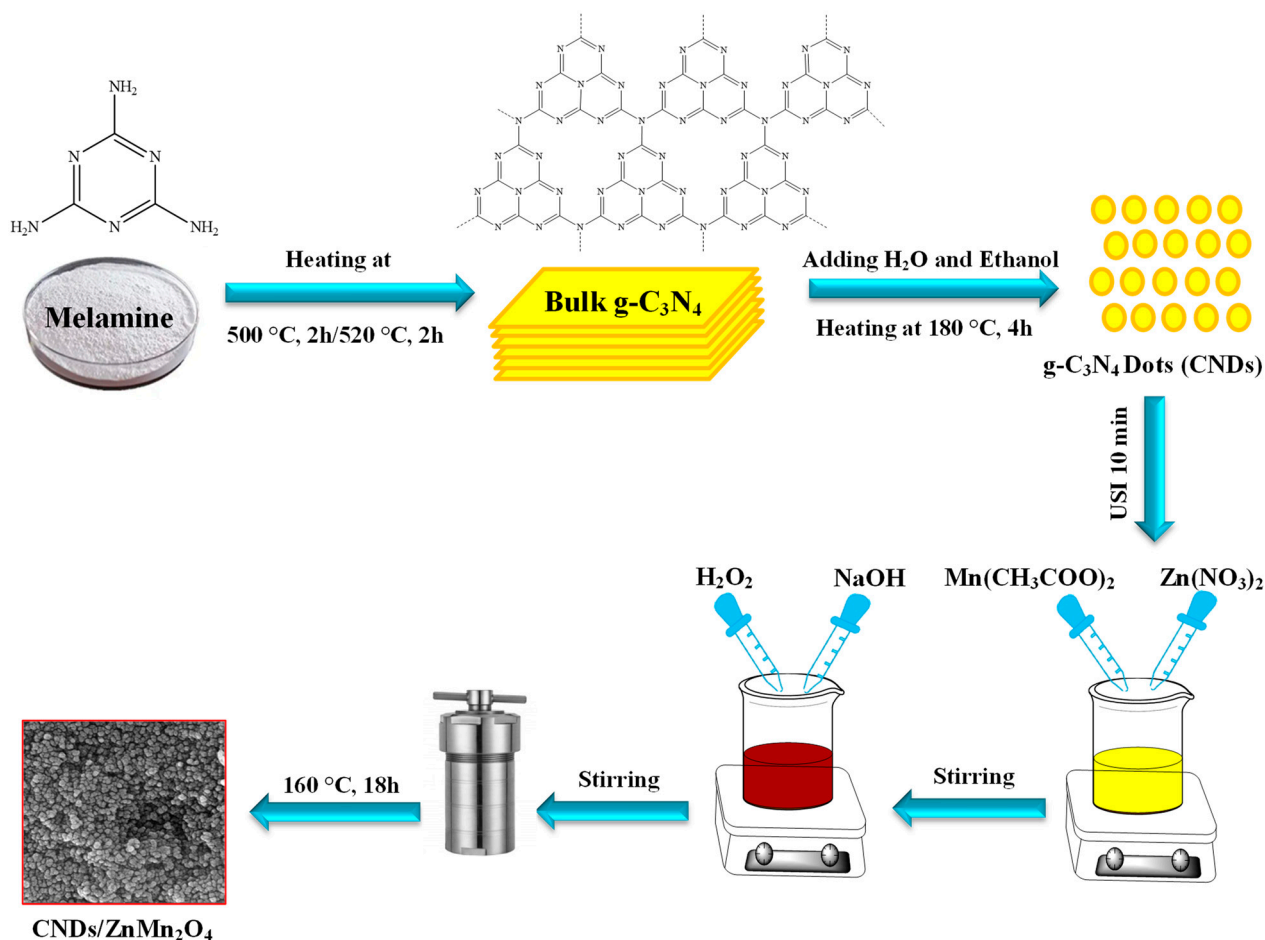
#### 3.1. Materials Section

The chemicals utilized in this research are melamine ( $C_3H_6N_6$ , 99%, Central Drug House), ethanol (96%, Merck),  $Zn(NO_3)_2 \cdot 6H_2O$  (96%, Loba Chemie),  $Mn(CH_3COO)_2 \cdot 4H_2O$  (99%, Merck), NaOH (98%, Merck),  $H_2O_2$  (35%, Neutron).

#### 3.2. Photocatalyst Synthesis

The CN was synthesized via the previously reported method [40]. For the synthesis of the CNs sample, the mixture of CN with 20 mL of ethanol was stirred for half an hour. Then the solution of 25 mL of water and 25 mL of ethanol was added dropwise to the previous mixture. After stirring for half an hour, it was heated at 180 °C for 4 h in an autoclave.

The CNs/ $ZnMn_2O_4$  systems were fabricated using a hydrothermal procedure (Scheme 1). For the synthesis of CNs/ $ZnMn_2O_4$  (20%) nanocomposite, as the optimal photocatalyst with the best performance, 0.4 g of CNs was mixed with 100 mL of  $H_2O$  under sonication for 10 min. Meanwhile, an aqueous solution of zinc nitrate ( $Zn(NO_3)_2 \cdot 6H_2O$ , Loba Chemie, 0.124 g in 10 mL  $H_2O$ ) was mixed with the above-obtained suspension, while stirring for 60 min at 25 °C. On the other hand, an aqueous solution of manganese (II) acetate ( $Mn(CH_3COO)_2 \cdot 4H_2O$ , Merck, 0.205 g in 10 mL  $H_2O$ ) was added to the resultant suspension and stirred for 60 min. At the next step, 20 mL NaOH (Merck, 0.4 M) and 1 mL  $H_2O_2$  (Neutron, 14.9 M) solutions were combined with the suspension under stirring for more 15 min. In the end, the suspension was heated in a stainless-steel autoclave for 18 h at 160 °C. After cooling and washing, the resultant composite was dried in an oven.



**Scheme 1.** Schematic illustration for the synthesis of CNs/ $ZnMn_2O_4$  photocatalysts.

### 3.3. Characterization Techniques

The EDX analyses and FESEM images were obtained by a Tescan Mira3 instrument. The XRD analyses were carried out on a Philips Xpert X-ray instrument with a Cu K $\alpha$  source. A Scinco 4100 spectrophotometer was employed to record the UV-vis DR spectra. The FT-IR spectra were collected on a PerkinElmer Spectrum RX I apparatus. A PerkinElmer LS 55 fluorescence spectrophotometer was employed to record the PL spectra. The concentration of the dye pollutants was determined by UV-vis spectrophotometer (Cecile 9000). The TEM and HRTEM images were photographed using a HighTech HT7700 (Tokyo, Japan) instrument. The XPS analyses were conducted by a Specs-Flex XPS (Berlin, Germany). A BELSORP mini II (York, PA, USA) instrument was applied to fulfill the N<sub>2</sub> adsorption-desorption measurements. A  $\mu$ AutolabIII/FRA2 EIS (Utrecht, The Netherlands) was employed to accomplish the electrochemical analyses. The results of photocurrent data were also obtained with  $\mu$ AutolabIII/FRA2.

### 3.4. Photodegradation Tests

The photodegradation experiments were conducted in a photoreactor including a glass reactor furnished with a water-circulating device, a magnetic bar, and an air-purging system. An installed LED lamp (50 W,  $\lambda = 450\text{--}650$  nm) on the top of the reactor supplied the visible light. For the experiments, the photocatalyst powder (0.1 g) was supplemented into 250 mL of the aqueous suspensions of the pollutant (RhB:  $1.0 \times 10^{-5}$  M, MB:  $1.0 \times 10^{-5}$  M, MG:  $1.0 \times 10^{-5}$  M, or fuchsin:  $1.0 \times 10^{-5}$  M), and vigorously stirred for 60 min in the absence of light to accomplish the adsorption-desorption equilibrium. Next, the lamp was switched on for a predetermined time and almost 4 mL of the suspension was sampled at fixed time pauses, and photocatalyst particles were separated using a centrifuge (at 4000 rpm). The concentrations of RhB, fuchsin, MG, and MB were monitored by a UV-vis spectrophotometer, respectively, at 553, 540, 610 and 664 nm. To show the stability of the nanocomposite, we performed the recycling tests for four times consecutively. After each photocatalysis experiment, the photocatalyst was removed and utilized in the next test. Furthermore, to identify the reactive species generated during the degradation of RhB, ammonium oxalate (AOX, h<sup>+</sup> quencher, 0.035 g), benzoquinone (BQ,  $\bullet\text{O}_2^-$  quencher, 0.027 g), and 2-propanol (2-PrOH,  $\bullet\text{OH}$  quencher, 20  $\mu\text{L}$ ) were added to the system to capture, respectively, h<sup>+</sup>,  $\bullet\text{O}_2^-$ , and  $\bullet\text{OH}$  species.

## 4. Conclusions

In brief, CNs/ZnMn<sub>2</sub>O<sub>4</sub> nanocomposites were synthesized via a facile hydrothermal route. The successful integration of ZnMn<sub>2</sub>O<sub>4</sub> nanoparticles over the CNs was confirmed by various analyses. The photodegradation experiments revealed that the prepared binary nanocomposites had higher efficiencies for degradations of the selected pollutants under visible light compared to the efficiencies of ZnMn<sub>2</sub>O<sub>4</sub>, CNs, and bulk CN photocatalysts. Amongst the binary photocatalysts, the nanocomposite with 20 wt.% of ZnMn<sub>2</sub>O<sub>4</sub> had admirable activity in the removal of RhB with degradation constant of  $747 \times 10^{-4} \text{ min}^{-1}$ , mainly resulting from the enhanced specific surface area, significant absorption of visible light, and premiere segregation and transfer of the photoinduced charge carriers through developed p-n heterojunction. Moreover, the activity of the binary sample for degradation of RhB, MG, fuchsin, and MB was 66.5, 15.8, 13.2, and 31.2-fold greater than CN, and 3.44, 1.5, 18.1, and 11.5 times premier than CNs, respectively. As per radical trapping experiments, the  $\bullet\text{O}_2^-$ , h<sup>+</sup>, and  $\bullet\text{OH}$  radicals were recognized as the core reactive species involved in the photocatalytic processes. The outcomes of this work disclosed that the combination of ZnMn<sub>2</sub>O<sub>4</sub> and CNs components through p-n heterojunction not only provoked better absorption efficiencies at visible-light region but also improved the lifespan of the photoinduced charges and their movement on the surface of the photocatalyst for promoted degradation of various organic contaminants.

**Author Contributions:** Z.L.: Validation; Formal analysis; Investigation; Resources; Writing—Original Draft. A.H.-Y.: Conceptualization; Methodology; Writing—Review & Editing; Supervision; Project administration. S.R.P.: Writing—Review & Editing. A.K.: Formal analysis; Review & Editing. All authors have read and agreed to the published version of the manuscript.

**Funding:** This research was supported by University of Mohaghegh Ardabili.

**Data Availability Statement:** The data will be available on request.

**Acknowledgments:** We are grateful to the University of Mohaghegh Ardabili for supporting this work.

**Conflicts of Interest:** Authors stated that there is no conflict of interest.

## References

1. Ramalingam, G.; Perumal, N.; Priya, A.; Rajendran, S. A review of graphene-based semiconductors for photocatalytic degradation of pollutants in wastewater. *Chemosphere* **2022**, *300*, 134391. [[CrossRef](#)]
2. Solangi, N.H.; Karri, R.R.; Mazari, S.A.; Mubarak, N.M.; Jatoi, A.S.; Malafaia, G.; Azad, A.K. MXene as emerging material for photocatalytic degradation of environmental pollutants. *Coord. Chem. Rev.* **2023**, *477*, 214965. [[CrossRef](#)]
3. He, J.; Han, L.; Wang, F.; Ma, C.; Cai, Y.; Ma, W.; Xu, E.G.; Xing, B.; Yang, Z. Photocatalytic strategy to mitigate microplastic pollution in aquatic environments: Promising catalysts, efficiencies, mechanisms, and ecological risks. *Crit. Rev. Environ. Sci. Technol.* **2022**, *53*, 504–526. [[CrossRef](#)]
4. Brillas, E. A critical review on ibuprofen removal from synthetic waters, natural waters, and real wastewaters by advanced oxidation processes. *Chemosphere* **2021**, *286*, 131849. [[CrossRef](#)] [[PubMed](#)]
5. Ganiyu, S.O.; Sable, S.; El-Din, M.G. Advanced oxidation processes for the degradation of dissolved organics in produced water: A review of process performance, degradation kinetics and pathway. *Chem. Eng. J.* **2021**, *429*, 132492. [[CrossRef](#)]
6. Ch-Th, T.; Manisekaran, R.; Santoyo-Salazar, J.; Schoefs, B.; Velumani, S.; Castaneda, H.; Jantrania, A. Graphene oxide decorated TiO<sub>2</sub> and BiVO<sub>4</sub> nanocatalysts for enhanced visible-light-driven photocatalytic bacterial inactivation. *J. Photochem. Photobiol. A Chem.* **2021**, *418*, 113374. [[CrossRef](#)]
7. Lin, J.; Tian, W.; Zhang, H.; Duan, X.; Sun, H.; Wang, H.; Fang, Y.; Huang, Y.; Wang, S. Carbon nitride-based Z-scheme heterojunctions for solar-driven advanced oxidation processes. *J. Hazard. Mater.* **2022**, *434*, 128866. [[CrossRef](#)] [[PubMed](#)]
8. Bai, L.; Huang, H.; Yu, S.; Zhang, D.; Huang, H.; Zhang, Y. Role of transition metal oxides in g-C<sub>3</sub>N<sub>4</sub>-based heterojunctions for photocatalysis and supercapacitors. *J. Energy Chem.* **2021**, *64*, 214–235. [[CrossRef](#)]
9. Huang, H.; Jiang, L.; Yang, J.; Zhou, S.; Yuan, X.; Liang, J.; Wang, H.; Wang, H.; Bu, Y.; Li, H. Synthesis and modification of ultrathin g-C<sub>3</sub>N<sub>4</sub> for photocatalytic energy and environmental applications. *Renew. Sustain. Energy Rev.* **2023**, *173*, 113110. [[CrossRef](#)]
10. Balakrishnan, A.; Chinthala, M. Comprehensive review on advanced reusability of g-C<sub>3</sub>N<sub>4</sub> based photocatalysts for the removal of organic pollutants. *Chemosphere* **2022**, *297*, 134190. [[CrossRef](#)]
11. Guo, R.T.; Wang, J.; Bi, Z.X.; Chen, X.; Hu, X.; Pan, W.G. Recent advances and perspectives of g-C<sub>3</sub>N<sub>4</sub>-based materials for photocatalytic dyes degradation. *Chemosphere* **2022**, *295*, 133834. [[CrossRef](#)] [[PubMed](#)]
12. Wang, T.; Nie, C.; Ao, Z.; Wang, S.; An, T. Recent progress in g-C<sub>3</sub>N<sub>4</sub> quantum dots: Synthesis, properties and applications in photocatalytic degradation of organic pollutants. *J. Mater. Chem. A* **2019**, *8*, 485–502. [[CrossRef](#)]
13. Ma, P.; Zhang, X.; Wang, C.; Wang, Z.; Wang, K.; Feng, Y.; Wang, J.; Zhai, Y.; Deng, J.; Wang, L.; et al. Band alignment of homojunction by anchoring CN quantum dots on g-C<sub>3</sub>N<sub>4</sub> (0D/2D) enhance photocatalytic hydrogen peroxide evolution. *Appl. Catal. B Environ.* **2021**, *300*, 120736. [[CrossRef](#)]
14. Xing, Y.; Wang, X.; Hao, S.; Zhang, X.; Ma, W.; Zhao, G.; Xu, X. Recent advances in the improvement of g-C<sub>3</sub>N<sub>4</sub> based photocatalytic materials. *Chin. Chem. Lett.* **2021**, *32*, 13–20. [[CrossRef](#)]
15. Huang, R.; Wu, J.; Zhang, M.; Liu, B.; Zheng, Z.; Luo, D. Strategies to enhance photocatalytic activity of graphite carbon nitride-based photocatalysts. *Mater. Des.* **2021**, *210*, 110040. [[CrossRef](#)]
16. Zhu, F.; Ma, J.; Ji, Q.; Cheng, H.; Komarneni, S. Visible-light-driven activation of sodium persulfate for accelerating orange II degradation using ZnMn<sub>2</sub>O<sub>4</sub> photocatalyst. *Chemosphere* **2021**, *278*, 130404. [[CrossRef](#)]
17. Al-Buriahi, A.K.; Al-Gheethi, A.A.; Kumar, P.S.; Mohamed, R.M.S.R.; Yusof, H.; Alsharif, A.F.; Khalifa, N.A. Elimination of rhodamine B from textile wastewater using nanoparticle photocatalysts: A review for sustainable approaches. *Chemosphere* **2022**, *287*, 132162. [[CrossRef](#)]
18. Li, S.-S.; Liu, M.; Wen, L.; Xu, Z.; Cheng, Y.-H.; Chen, M.-L. Exploration of long afterglow luminescent materials composited with graphitized carbon nitride for photocatalytic degradation of basic fuchsin. *Environ. Sci. Pollut. Res.* **2023**, *30*, 322–336. [[CrossRef](#)]
19. Tsvetkov, M.; Zaharieva, J. Milanova, Ferrites, modified with silver nanoparticles, for photocatalytic degradation of malachite green in aqueous solutions. *Catal. Today* **2020**, *357*, 453–459. [[CrossRef](#)]
20. Khan, I.; Saeed, K.; Zekker, I.; Zhang, B.; Hendi, A.H.; Ahmad, A.; Ahmad, S.; Zada, N.; Ahmad, H.; Shah, L.A.; et al. Review on Methylene Blue: Its Properties, Uses, Toxicity and Photodegradation. *Water* **2022**, *14*, 242. [[CrossRef](#)]

21. Li, Y.; Shu, S.; Huang, L.; Liu, J.; Liu, J.; Yao, J.; Liu, S.; Zhu, M.; Huang, L. Construction of a novel double S-scheme structure  $\text{WO}_3/\text{g-C}_3\text{N}_4/\text{BiOI}$ : Enhanced photocatalytic performance for antibacterial activity. *J. Colloid Interface Sci.* **2023**, *633*, 60–71. [[CrossRef](#)] [[PubMed](#)]
22. Jing, Y.; Chen, Z.; Ding, E.; Yuan, R.; Liu, B.; Xu, B.; Zhang, P. High-yield production of  $\text{g-C}_3\text{N}_4$  quantum dots as photocatalysts for the degradation of organic pollutants and fluorescent probes for detection of  $\text{Fe}^{3+}$  ions with live cell application. *Appl. Surf. Sci.* **2022**, *586*, 152812. [[CrossRef](#)]
23. Basaleh, A.S.; Mohamed, R.M. Influence of doped silver nanoparticles on the photocatalytic performance of  $\text{ZnMn}_2\text{O}_4$  in the production of methanol from  $\text{CO}_2$  photocatalytic reduction. *Appl. Nanosci.* **2020**, *10*, 3865–3874. [[CrossRef](#)]
24. Wei, Y.; Li, X.; Zhang, Y.; Yan, Y.; Huo, P.; Wang, H.  $\text{G-C}_3\text{N}_4$  quantum dots and Au nano particles co-modified  $\text{CeO}_2/\text{Fe}_3\text{O}_4$  micro-flowers photocatalyst for enhanced  $\text{CO}_2$  photoreduction. *Renew. Energy* **2021**, *179*, 756–765. [[CrossRef](#)]
25. Preeyanghaa, M.; Vinesh, V.; Sabarikirishwaran, P.; Rajkamal, A.; Ashokkumar, M.; Neppolian, B. Investigating the role of ultrasound in improving the photocatalytic ability of CQD decorated boron-doped  $\text{g-C}_3\text{N}_4$  for tetracycline degradation and first-principles study of nitrogen-vacancy formation. *Carbon* **2022**, *192*, 405–417. [[CrossRef](#)]
26. He, L.; Fei, M.; Chen, J.; Tian, Y.; Jiang, Y.; Huang, Y.; Xu, K.; Hu, J.; Zhao, Z.; Zhang, Q.; et al. Graphitic  $\text{C}_3\text{N}_4$  quantum dots for next-generation QLED displays. *Mater. Today* **2018**, *22*, 76–84. [[CrossRef](#)]
27. Xu, C.; Li, D.; Liu, X.; Ma, R.; Sakai, N.; Yang, Y.; Lin, S.; Yang, J.; Pan, H.; Huang, J.; et al. Direct Z-scheme construction of  $\text{g-C}_3\text{N}_4$  quantum dots/ $\text{TiO}_2$  nanoflakes for efficient photocatalysis. *Chem. Eng. J.* **2021**, *430*, 132861. [[CrossRef](#)]
28. Yan, S.; Yanlong, Y.; Cao, Y. Synthesis of porous  $\text{ZnMn}_2\text{O}_4$  flower-like microspheres by using MOF as precursors and its application on photoreduction of  $\text{CO}_2$  into CO. *Appl. Surf. Sci.* **2019**, *465*, 383–388. [[CrossRef](#)]
29. Olusegun, S.J.; Larrea, G.; Osial, M.; Jackowska, K.; Krysinski, P. Photocatalytic Degradation of Antibiotics by Superparamagnetic Iron Oxide Nanoparticles. Tetracycline Case. *Catalysts* **2021**, *11*, 1243. [[CrossRef](#)]
30. Papadas, I.T.; Galatopoulos, F.; Armatas, G.S.; Tessler, N.; Choulis, S.A. Nanoparticulate Metal Oxide Top Electrode Interface Modification Improves the Thermal Stability of Inverted Perovskite Photovoltaics. *Nanomaterials* **2019**, *9*, 1616. [[CrossRef](#)]
31. Alhaddad, M.; Mohamed, R.M. Synthesis and characterizations of  $\text{ZnMn}_2\text{O}_4\text{-ZnO}$  nanocomposite photocatalyst for enlarged photocatalytic oxidation of ciprofloxacin using visible light irradiation. *Appl. Nanosci.* **2020**, *10*, 2269–2278. [[CrossRef](#)]
32. Wu, X.; Xiang, Y.; Peng, Q.; Wu, X.; Li, Y.; Tang, F.; Song, R.; Liu, Z.; He, Z.; Wu, X. Green-low-cost rechargeable aqueous zinc-ion batteries using hollow porous spinel  $\text{ZnMn}_2\text{O}_4$  as the cathode material. *J. Mater. Chem. A* **2017**, *5*, 17990–17997. [[CrossRef](#)]
33. Ni, Q.; Cheng, H.; Ma, J.; Kong, Y.; Komarneni, S. Efficient degradation of orange II by  $\text{ZnMn}_2\text{O}_4$  in a novel photo-chemical catalysis system. *Front. Chem. Sci. Eng.* **2020**, *14*, 956–966. [[CrossRef](#)]
34. Iurilli, P.; Brivio, C.; Wood, V. On the use of electrochemical impedance spectroscopy to characterize and model the aging phenomena of lithium-ion batteries: A critical review. *J. Power Sources* **2021**, *505*, 229860. [[CrossRef](#)]
35. Schlumberger, C.; Thommes, M. Characterization of Hierarchically Ordered Porous Materials by Physisorption and Mercury Porosimetry—A Tutorial Review. *Adv. Mater. Interfaces* **2021**, *8*, 2002181. [[CrossRef](#)]
36. Deng, H.; Fei, X.; Yang, Y.; Fan, J.; Yu, J.; Cheng, B.; Zhang, L. S-scheme heterojunction based on p-type  $\text{ZnMn}_2\text{O}_4$  and n-type ZnO with improved photocatalytic  $\text{CO}_2$  reduction activity. *Chem. Eng. J.* **2020**, *409*, 127377. [[CrossRef](#)]
37. Wang, A.; Guo, S.; Zheng, Z.; Wang, H.; Song, X.; Zhu, H.; Zeng, Y.; Lam, J.; Qiu, R.; Yan, K. Highly dispersed Ag and  $\text{g-C}_3\text{N}_4$  quantum dots co-decorated 3D hierarchical  $\text{Fe}_3\text{O}_4$  hollow microspheres for solar-light-driven pharmaceutical pollutants degradation in natural water matrix. *J. Hazard. Mater.* **2022**, *434*, 128905. [[CrossRef](#)]
38. Khan, I.; Saeed, K.; Ali, N.; Khan, I.; Zhang, B.; Sadiq, M. Heterogeneous photodegradation of industrial dyes: An insight to different mechanisms and rate affecting parameters. *J. Environ. Chem. Eng.* **2020**, *8*, 104364. [[CrossRef](#)]
39. Ahmad, S.; Almeahadi, M.; Janjuhah, H.T.; Kontakiotis, G.; Abdulaziz, O.; Saeed, K.; Ahmad, H.; Allahyani, M.; Aljuaid, A.; Alsaiani, A.A.; et al. The Effect of Mineral Ions Present in Tap Water on Photodegradation of Organic Pollutants: Future Perspectives. *Water* **2023**, *15*, 175. [[CrossRef](#)]
40. Yin, Y.; Liu, M.; Shi, L.; Zhang, S.; Hirani, R.A.K.; Zhu, C.; Chen, C.; Yuan, A.; Duan, X.; Wang, S.; et al. Highly dispersive Ru confined in porous ultrathin  $\text{g-C}_3\text{N}_4$  nanosheets as an efficient peroxydisulfate activator for removal of organic pollutants. *J. Hazard. Mater.* **2022**, *435*, 128939. [[CrossRef](#)]

**Disclaimer/Publisher’s Note:** The statements, opinions and data contained in all publications are solely those of the individual author(s) and contributor(s) and not of MDPI and/or the editor(s). MDPI and/or the editor(s) disclaim responsibility for any injury to people or property resulting from any ideas, methods, instructions or products referred to in the content.